





# Digital light 3D printing of customized bioresorbable airway stents with elastomeric properties

## Journal Article

### Author(s):

Paunović, Nevena; Bao, Yinyin; [Coulter, Fergal Brian](#) ; [Masania, Kunal](#) ; Geks, Anna K.; Klein, Karina; Rafsanjani, Ahmad; Cadalbert, Jasmin; Kronen, Peter W.; Kleger, Nicole; Karol, Agnieszka; [Luo, Zhi](#) ; Rüber, Fabienne; Brambilla, Davide; von Rechenberg, Brigitte; Franzen, Daniel; Studart, André R.; [Leroux, Jean-Christophe](#) 

### Publication date:

2021

### Permanent link:

<https://doi.org/10.3929/ethz-b-000472086>

### Rights / license:

[Creative Commons Attribution 4.0 International](#)

### Originally published in:

Science Advances 7(6), <https://doi.org/10.1126/sciadv.abe9499>

## ENGINEERING

# Digital light 3D printing of customized bioresorbable airway stents with elastomeric properties

Nevena Paunović<sup>1\*</sup>, Yinyin Bao<sup>1\*</sup>, Fergal Brian Coulter<sup>2</sup>, Kunal Masania<sup>2,3</sup>, Anna Karoline Geks<sup>4</sup>, Karina Klein<sup>4</sup>, Ahmad Rafsanjani<sup>2,5</sup>, Jasmin Cadalbert<sup>1</sup>, Peter W. Kronen<sup>4,6,7</sup>, Nicole Kleger<sup>2</sup>, Agnieszka Karol<sup>4</sup>, Zhi Luo<sup>1</sup>, Fabienne Rüber<sup>8</sup>, Davide Brambilla<sup>1,9</sup>, Brigitte von Rechenberg<sup>4</sup>, Daniel Franzen<sup>8†</sup>, André R. Studart<sup>2†</sup>, Jean-Christophe Leroux<sup>1†</sup>

Central airway obstruction is a life-threatening disorder causing a high physical and psychological burden to patients. Standard-of-care airway stents are silicone tubes, which provide immediate relief but are prone to migration. Thus, they require additional surgeries to be removed, which may cause tissue damage. Customized bioresorbable airway stents produced by 3D printing would be highly needed in the management of this disorder. However, biocompatible and biodegradable materials for 3D printing of elastic medical implants are still lacking. Here, we report dual-polymer photoinks for digital light 3D printing of customized and bioresorbable airway stents. These stents exhibit tunable elastomeric properties with suitable biodegradability. In vivo study in healthy rabbits confirmed biocompatibility and showed that the stents stayed in place for 7 weeks after which they became radiographically invisible. This work opens promising perspectives for the rapid manufacturing of the customized medical devices for which high precision, elasticity, and degradability are sought.

## INTRODUCTION

Central airway obstruction (CAO) is a stenosis of the trachea or mainstem bronchi that causes impaired air flow and has immense impact on morbidity and mortality (1, 2). Immediate relief in patients suffering from CAO can be provided after bronchoscopic insertion of airway stents, which are life-saving medical devices designed to restore the anatomical shape of the airways (3). The most widely used airway stents are made from flexible and elastic biocompatible medical-grade silicone. However, the commercial silicone stents are simple tubes associated with a high risk of migration due to geometrical mismatching with the complex tracheobronchial anatomy of the individual patient (1, 3). This is especially noticeable in pediatric patients who need additional interventions for stent removal or replacement due to the airway growth, which may cause further tissue damage (1, 4). Therefore, there is an unmet medical need for affordable patient-specific bioresorbable airway stents that can be manufactured in a reasonable time frame (1, 3). Nonetheless, conventional manufacturing technologies of airway stents make personalization expensive and time-consuming (5).

In combination with imaging techniques, three-dimensional (3D) printing technologies (6–13) provide enormous opportunities for rapid and affordable production of personalized medical devices (14–17). Nonetheless, their use in medicine is restricted by the lack of biocompatible and biodegradable materials that are suitable for

the 3D printing of medical devices with silicone-like mechanical properties. So far, 3D printed bioresorbable airway stents have been made from thermoplastic polymers by fused deposition modeling and are prone to stress relaxation or even permanent deformation when being constrained before insertion (5, 18). These challenges could be overcome by digital light processing (DLP) of highly stretchable elastomers. While DLP offers the benefit of high resolution and surface quality (6, 19, 20) compared to other 3D printing techniques, it also heavily depends on the resin viscosity (21, 22). Therefore, only biodegradable oligomers or polymers with short chain length have been used to prepare DLP biomedical inks, and these produce rigid and brittle 3D printed objects (23–25). Hence, the development of inks for DLP 3D printing of biodegradable elastomers with mechanical properties comparable to silicone stents would be a big step forward to clinical application of personalized bioresorbable airway stents.

Here, we report dual-polymer DLP biomedical inks based on functionalized poly(D,L-lactide-co-ε-caprolactone)s [poly(DLLA-co-CL)s], which are suitable for 3D printing of bioresorbable elastomers. The most promising material was identified on the basis of successive testing of mechanical performance, cytocompatibility, and degradability at physiological pH and further used to 3D print customized bioresorbable airway stents with elastomeric properties comparable to those of commercial state-of-the-art silicone stents (Fig. 1). This work proposes a blueprint for the design, manufacturing, characterization, and assessment of the next generation of airway stents (Fig. 1) that could, in the future, meet patients' needs in terms of both geometry and bioresorbability.

## RESULTS

### Design and optimization of the biomedical inks

To obtain biodegradable polymers in a liquid state at ambient temperature, two distinct monomers, i.e., D,L-lactide (DLLA) and ε-caprolactone (CL), were copolymerized (26). The random copolymerization results in amorphous copolymers with lower viscosity

<sup>1</sup>Institute of Pharmaceutical Sciences, Department of Chemistry and Applied Biosciences, ETH Zurich, Zurich, Switzerland. <sup>2</sup>Complex Materials, Department of Materials, ETH Zurich, Zurich, Switzerland. <sup>3</sup>Shaping Matter Lab, Faculty of Aerospace Engineering, TU Delft, Delft, Netherlands. <sup>4</sup>Musculoskeletal Research Unit, Vetsuisse Faculty, University of Zurich, Zurich, Switzerland. <sup>5</sup>SDU Biorobotics, The Mærsk Mc-Kinney Møller Institute, University of Southern Denmark, Odense, Denmark. <sup>6</sup>Veterinary Anaesthesia Services-International, Winterthur, Switzerland. <sup>7</sup>Center for Applied Biotechnology and Molecular Medicine, University of Zurich, Zurich, Switzerland. <sup>8</sup>Department of Pulmonology, University Hospital Zurich, Zurich, Switzerland. <sup>9</sup>Faculty of Pharmacy, Université de Montréal, Montréal, QC, Canada.

\*These authors contributed equally to this work.

†Corresponding author. Email: daniel.franzen@usz.ch (D.F.); andre.studart@mat.ethz.ch (A.R.S.); jleroux@ethz.ch (J.-C.L.)

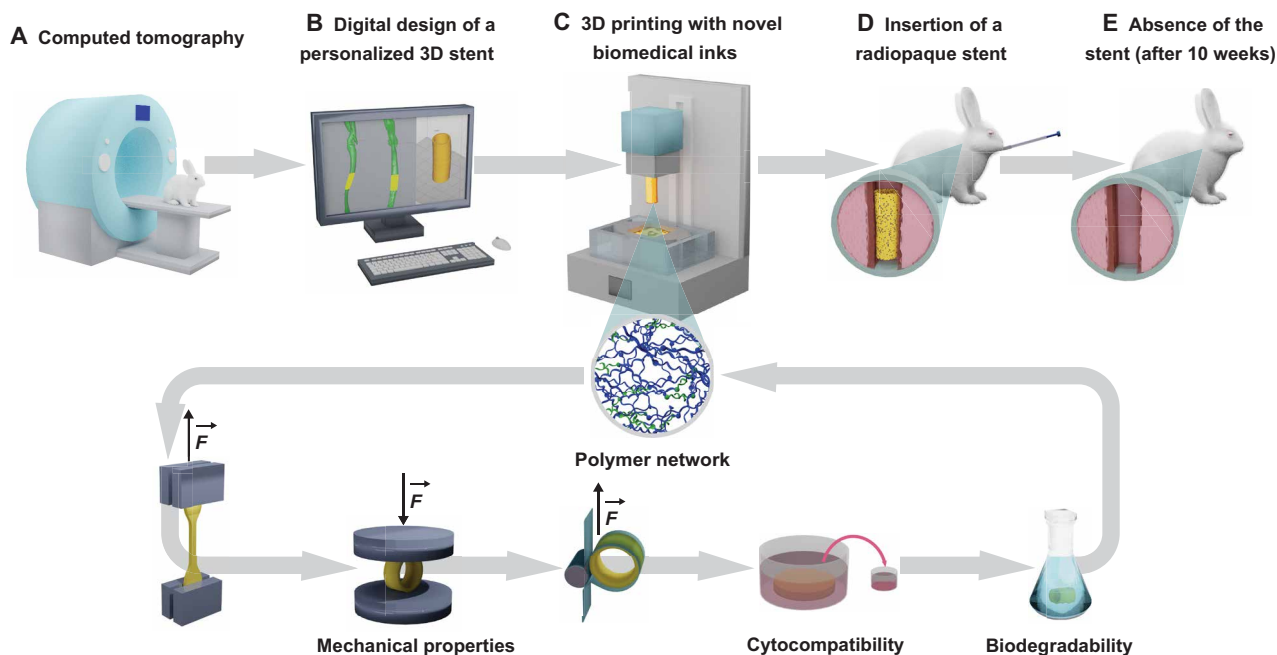


**Fig. 1. Schematic workflow for manufacturing and testing of bioresorbable, biocompatible, and customized airway stents by DLP 3D printing.** (A) A 3D model of the rabbit trachea was created from computed tomography scan images. (B) The customized stent was designed to match the tracheal geometry and surface topology. (C) Biomedical inks were developed by mixing photopolymerizable random copolymers of high (in blue) and low (in green) molecular weight (inset). The most promising 3D printed material, which was identified on the basis of successive testing of mechanical performance, cytocompatibility, and degradability, was used to manufacture bioresorbable customized stents by DLP. (D) The stents were then made radiopaque by postprinting gold incorporation and inserted in New Zealand white rabbits with an in-house-developed delivery device. (E) The rabbits were radiographically monitored over 10 weeks, and no stent was present in a respiratory tract upon completion of the study.

than homopolymers of the same molecular weight (MW) (24, 26, 27). As branched polymers generally show lower viscosity (28) and higher cross-linking density together with better mechanical properties (29) than the linear ones, a series of four-arm poly(DLLA-*co*-CL)s was synthesized by Sn(Oct)<sub>2</sub>-catalyzed ring opening polymerization at 140°C, with a molar feed ratio DLLA/CL of 3/7 and MW ranging from 1200 to 15,000 g mol<sup>-1</sup>. These copolymers were further functionalized with methacrylates (degree of methacrylation ca. 80%) to make them suitable for photopolymerization (fig. S1). All photopolymers were amorphous (fig. S2) and liquid at room temperature. However, the viscosity of the copolymers with longer chain length (MW > 5000 g mol<sup>-1</sup>) was still above the range required for DLP printing (fig. S3A) (21). To tackle this issue, we designed a customized temperature-controlled printing platform that allows for a reduction in the polymer viscosity by heating the resin tray (fig. S4). Printing at temperatures in the range of 70 to 90°C effectively decreased the viscosity of the photopolymers without causing thermocuring under the tested conditions (fig. S3). This approach could be used for high-resolution printing of even high-MW photopolymers if up to 8 (weight %) wt % of the reactive diluent *N*-vinyl-2-pyrrolidone (NVP) was added to the resin. Furthermore, the composition of the printing resin was optimized to achieve minimal amounts of additives, such as photoinitiator [phenylbis(2,4,6-trimethyl-benzoyl)phosphine oxide, BAPO] and light-absorbing dye (Sudan I), while maintaining the printing resolution and the mechanical properties within suitable ranges (fig. S5).

Although the biocompatibility and biodegradability of the resin components are of primary importance, suitable mechanical properties are essential for the proper function and performance of the

printed stents. The mechanical properties of the printed object are defined by the chain length of the (macro)monomers and the cross-linking density of the polymer network created upon illumination (30, 31). To investigate the impact of photopolymer chain length on the mechanical properties of 3D printed objects, tensile tests were performed (fig. S6). The results indicated that the mechanical response of printed materials shifted from stiff and brittle to flexible and elastic with increasing MW and chain length of the copolymer. This was manifested by a gradual increase in elongation at break from ca. 30 to 150% and a reduction in Young's modulus from 43.6 to 2.9 MPa, as the MW increased from 1200 to 15,000 g mol<sup>-1</sup>. The photopolymer of 15,000 g mol<sup>-1</sup> (**P1**) was found to be most suitable for the intended application, owing to the highest elasticity among the tested materials provided by the long and flexible polymer chains.

The elastic polymer **P1** reached ultimate true tensile stress of ca. 10 MPa, which is still an order of magnitude lower than the value obtained for commercial silicone rubber of airway stents (fig. S7). To further improve the mechanical performance of the DLP printed material, a dual-polymer resin was designed by combining the polymer **P1** [number-average molecular weight ( $M_n$ ), NMR = 15,000 g mol<sup>-1</sup>] with a linear oligomer **P2** ( $M_n$ , NMR = 600 g mol<sup>-1</sup>, equimolar ratio of DLLA to CL; 2,2-diethyl-1,3-propanediol as the initiator), as presented in Fig. 2A. The addition of the polymer **P2** reduced the viscosity of the resin from ca. 10 to 5 Pa s at the printing temperature of 80°C (fig. S3B) and increased the cross-linking density of the formed network (fig. S8). This increased the ultimate true tensile stress of **P1** from 10 to 25 MPa if a **P1/P2** weight feed ratio of 75/25 was used in the printing resin (Fig. 2B). All materials remained elastic,

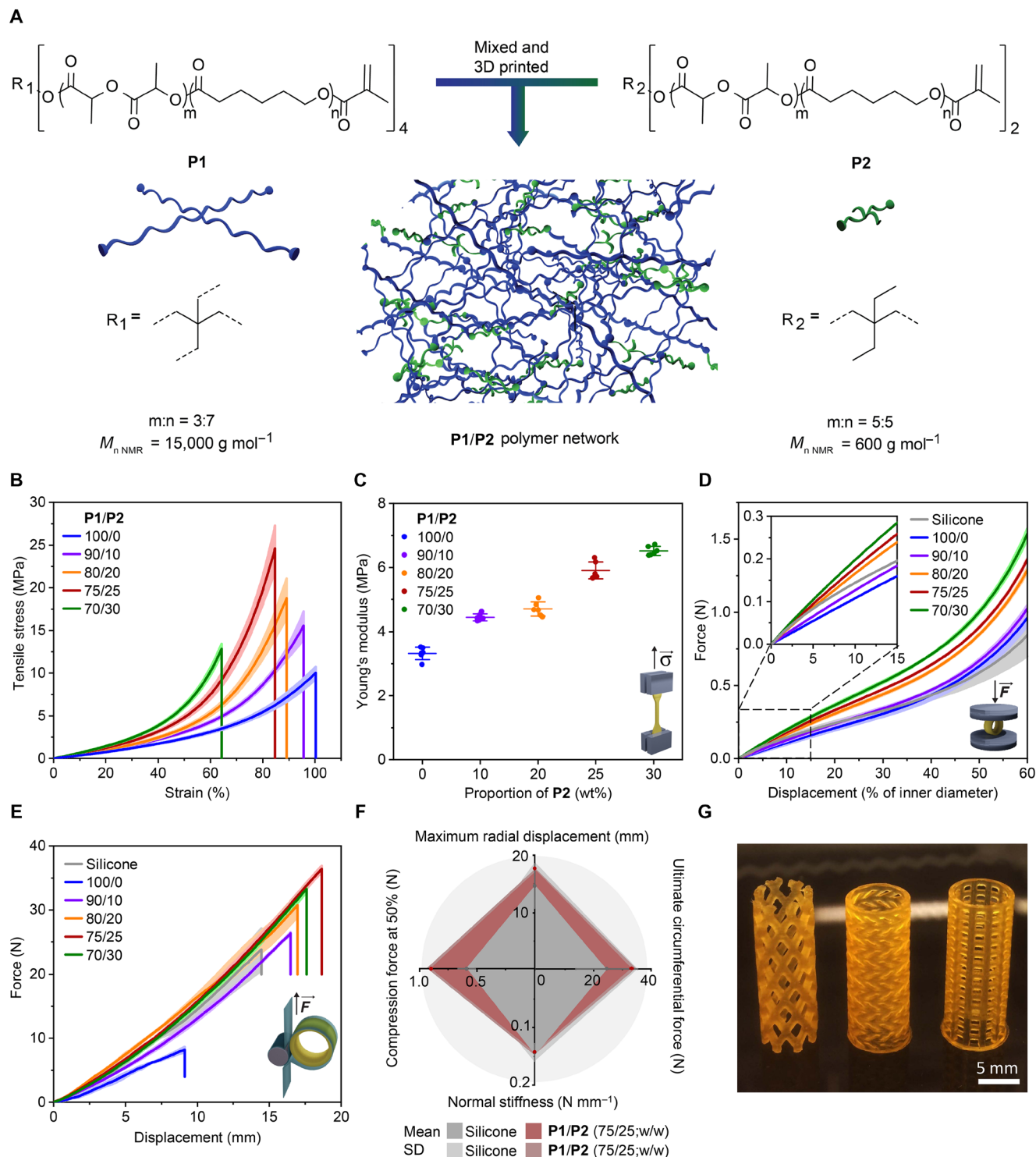


**Fig. 2. Mechanical performance of 3D printed materials based on P1/P2 dual-polymer resins with various proportions of P2.** (A) Schematic of the strategy for 3D printing of materials with dual-polymer resins. (B) Average true stress-strain tensile curves of materials produced with P1/P2 dual and P1 polymer resins. Mean  $\pm$  SD ( $n=6$ ). (C) Average Young's modulus of materials containing P1 with various amounts of P2. Mean  $\pm$  SD ( $n=6$ ). (D) Force-displacement curves of tubular specimens printed with P1/P2 dual-polymer resins and a NOVATECH silicone stent ( $H$  of 10.0 mm,  $\varnothing$  of 16.0 mm, and thickness of 1.2 mm), obtained in uniaxial compression tests. Inset: Force-displacement curves at low displacement (up to 15%). Mean  $\pm$  SD (one stent at three different positions). (E) Force-displacement curves obtained in Mylar loop experiments. Mean  $\pm$  SD (one stent at three different positions). (F) Comparison of mean values of key mechanical properties between NOVATECH silicone specimens (in gray) and DLP printed specimens from 75/25 (w/w) P1/P2 resin (in red) + SD (light gray and red, respectively) from  $n=6$ . Maximum radial displacement, ultimate circumferential force, normal stiffness, and force exerted at the displacement corresponding to 50% of the inner diameter in the uniaxial compression test were selected as application-relevant mechanical properties. (G) Stents of different designs DLP 3D printed with 75/25 (w/w) P1/P2 resin. Photo credit: Yinyin Bao, ETH Zurich.

with Young's modulus of ca. 3 to 6 MPa (Fig. 2C) and elongation at break above 60% (Fig. 2B).

Despite their lower tensile properties compared to silicone, our polymer networks shaped in stent-like tubular geometries were found to be sufficiently strong to withstand the high stress levels developed during radial compression and crimping. Resistance to buckling failure during radial compression and crimping is an essential requirement to ensure that airway stents are functional and can be loaded in the delivery device. Therefore, a series of nonmeshed tubular stents with size and shape corresponding to a NOVATECH silicone stent (height,  $H$  of 10.0 mm; diameter,  $\varnothing$  of 16.0 mm; and thickness of 1.2 mm) were printed with our polymer blends and tested in two application-relevant loading configurations (Fig. 2, D and E). Uniaxial compression tests revealed that all polymer-based stents show higher load-bearing capacity than the silicone stent for displacements above 50% of their inner diameter (Fig. 2D). No buckling was observed during this test. To quantify the circumferential (hoop) forces developed during radial compression, a custom Mylar loop was designed (fig. S9) (32). All stents, except pure P1, showed similar force-displacement curves and buckling modes preceding crimping (Fig. 2E). On the basis of the optimal combination of high uniaxial compression resistance, circumferential forces, and displacements before crimping, the 75/25 (w/w) P1/P2 polymer blend was selected for all further experiments. The 3D printed material of this composition displayed almost 1.5 times higher maximum circumferential force, 20% larger maximal radial displacement, and 1.5 times higher uniaxial compression resistance at larger displacements compared to the NOVATECH silicone stent, while keeping a comparable normal stiffness of ca.  $0.15 \text{ N mm}^{-1}$  (Fig. 2F). The high resolution and smooth surface quality achievable with the DLP 3D printing are demonstrated by

manufacturing tubular objects with distinct designs (33) using the optimal polymer blend (Fig. 2G).

Besides the properties of the constituent polymers, the mechanical performance of airway stents is also affected by geometrical parameters such as radius and wall thickness. To better understand the impact of geometry on the mechanical response of modeled tubular stents, we conducted finite element (FE) simulations on human-sized structures subjected to uniaxial compression (Fig. 3A). Using experimental data from tensile tests as input parameters, we found a very good fit of the numerical force-displacement curves to the experimental behavior of the tubular structures, confirming the validity of the computational analyses. Numerical snapshots of 75/25 (w/w) P1/P2-based stents during the uniaxial compression simulations (Fig. 3B) indicated no buckling of the tubes at high displacements, which is in accordance with the mechanical response observed in uniaxial compression experiments. The good agreement between experiments and simulations allowed us to apply the numerical tool to study the impact of radius and wall thickness on the normal stiffness of the stents based on 75/25 (w/w) P1/P2 3D printed materials. The simulation results revealed that the normal stiffness can change by as much as one order of magnitude by varying the radius and thickness within a range that is accessible by DLP 3D printing (Fig. 3C). Therefore, our analysis provides a design guide to determine the thickness needed to achieve the desired normal stiffness for a stent with the patient-defined radius.

### Cytocompatibility and in vitro degradation profile

The objects with the best mechanical properties that were 3D printed with 75/25 (w/w) P1/P2 were tested for cytocompatibility on human lung epithelial cells (A549). In compliance with International Organization for Standardization (ISO) standards (10993-5:2009 and

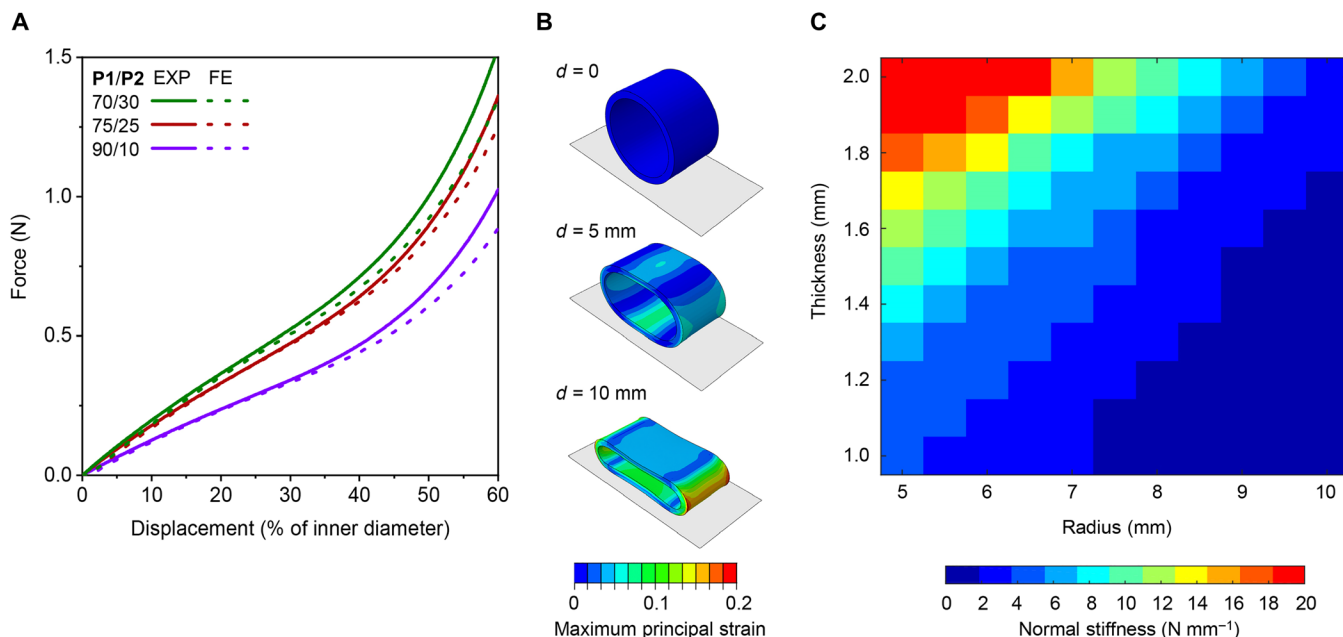


**Fig. 3. Numerical analysis of the mechanical properties of 3D printed materials based on P1/P2 dual-polymer resins.** (A) Comparison between experimental (EXP) and numerical (FE) force-displacement curves of tubular specimens ( $H$  of 10.0 mm,  $\varnothing$  of 16.0 mm, and thickness of 1.2 mm) 3D printed with P1/P2 (70/30, 75/25, and 90/10; w/w) dual-polymer resins. (B) Snapshots of a 75/25 (w/w) P1/P2-based tubular specimen ( $H$  of 10.0 mm,  $\varnothing$  of 16.0 mm, and thickness of 1.2 mm) compressed between two rigid plates at different displacements (0, 5, and 10 mm; from top to bottom). The colors represent the distribution of the maximum principal strains. (C) Contour plot of normal stiffness with the variations of radius and thickness of the 75/25 (w/w) P1/P2-based stent ( $H$  of 10.0 mm). The colored scale indicates normal stiffness.

10993-12:2009) for the development of medical devices, the medium extracts of produced materials were used as medium for the cells (34, 35). In addition, we developed a procedure in which 3D printed materials were placed on top of Transwell inserts to be directly immersed in the cell medium. Cell viability was determined by the MTS assay and compared to medium control. Incubation of A549 cells with the medium extracts of the 3D printed materials or 3D

printed materials in Transwell inserts did not significantly affect cell viability (Fig. 4A).

To study the degradation of our customized material, we 3D printed nonmeshed tubular structures as stent prototypes ( $H$  of 10.0 mm,  $\varnothing$  of 8.0 mm, and thickness of 1.0 mm) and incubated them in phosphate-buffered saline (PBS) buffer (pH 7.4) at 37° and 50°C. As shown in Fig. 4B, the stents underwent substantial weight loss in

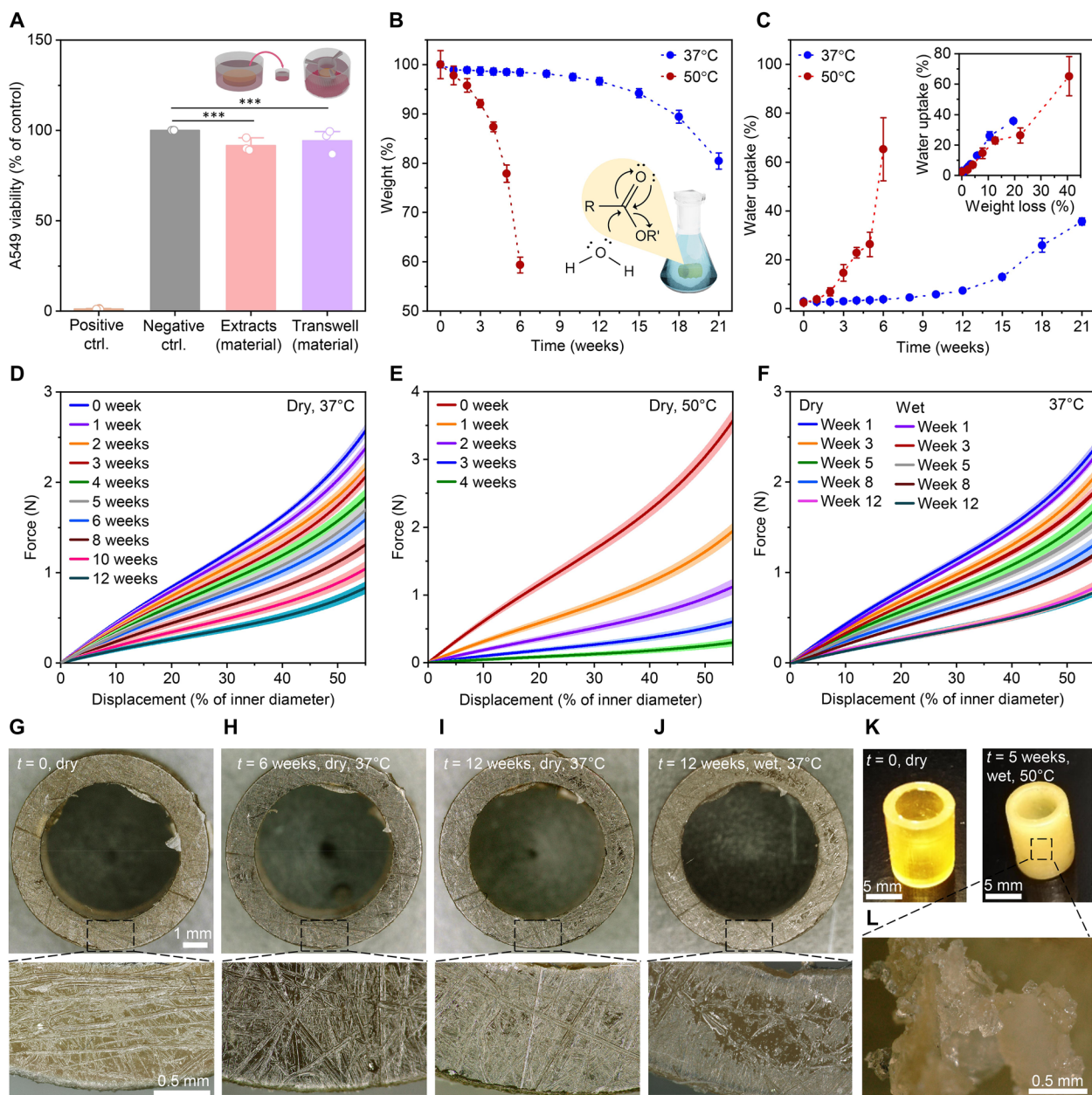


**Fig. 4. Cytocompatibility and degradation profile of 3D printed specimens based on 75/25 (w/w) P1/P2 dual-polymer resin.** (A) A549 viability demonstrated by the MTS assay compared to the medium control (gray bar). Positive control (10 mM hydrogen peroxide) is presented with an orange bar. Mean + SD ( $n=3$ ). Statistical significance was calculated by one-way analysis of variance (ANOVA) with Tukey's comparison test with  $***P < 0.001$ . (B and C) Changes in dry weight (B) and water uptake (C) of 3D printed stent prototypes ( $H$  of 10.0 mm,  $\varnothing$  of 8.0 mm, and thickness of 1.0 mm) over time following incubation in phosphate-buffered saline (PBS) buffer (pH 7.4) at 37° and 50°C. Inset (C): Water uptake in dependence of dry weight loss. (D and E) Compression curves of 3D printed stents incubated at 37° (D) and 50°C (E) at different time points. The tests were performed with the dried stents. (F) Compression curves in wet and dry states obtained with samples incubated at 37°C at various time points. (G to J) A representative stent during the degradation study at 37°C. (K and L) A representative stent from the degradation study at 50°C: intact (K, right) and upon breakage (L). (B to F) All data are expressed as means  $\pm$  SD ( $n=4$ ). Photo credit: Nevena Paunović, ETH Zurich.

accelerated degradation study (in red), with 60% of mass remaining after 6 weeks of incubation. At physiological temperature (in blue), almost no degradation was observed during that time. Degradation of the stents at 37°C became more evident from the fourth month, with weight loss reaching 20% after 5 months. These data were in line with the swelling of the stents (Fig. 4C), where weight ratio of water in the stents increased much faster at 50°C as compared to 37°C, reaching 70% of stent's weight after 6 weeks. When comparing the water uptake levels at the same weight loss level (e.g., 20%), similar water uptake was observed (30 to 40%). To evaluate the changes in the mechanical performance of the stents during the degradation, all stents were characterized by uniaxial compression test at different time points. The compression curves of dry stents incubated at 37°C (Fig. 4D) revealed ca. 50% loss in compressive force over 6 weeks, while those at 50°C (Fig. 4E) lost their mechanical properties completely within 4 weeks. As illustrated in Fig. 4F, the stents incubated at physiological temperature displayed almost no or minor differences in compression force between the dry and the wet states. These stents also maintained their dimensions and surface morphology over 12 weeks (Fig. 4, G to I, and fig. S10) and were unaffected by water uptake up to ca. 10% (Fig. 4, I and J, and fig. S10). In line with the previous experiments (Fig. 4C), degradation at 50°C resulted in opaque hydrogel-like stents after 5 weeks (Fig. 4, K and L).

### In vivo study in a rabbit model

In a pilot study, the insertion, tolerance, persistence, and bioresorbability of the customized DLP 3D printed airway stents prepared with the 75/25 (w/w) P1/P2 resin were assessed in healthy New Zealand white rabbits. Rabbits are commonly used in studies on airway stents because of the histological similarities of their tracheas with those of humans (36–41). Notably, a rabbit's trachea is more sensitive to compressive forces (42) and its epithelium is more reactive (43), making the tissue response to a stent faster and more extensive compared to humans. An average rabbit's trachea was created on the basis of computed tomography (CT) images of six rabbits. We designed customized round and slightly flattened stents fitting the model (length of 17 mm,  $\varnothing$  of 6.3 to 6.7 mm, and thickness of 0.6 mm) and oversized them by 15% (36) in diameter to prevent stent migration in vivo (Fig. 5A). The resulting 3D printed stents showed high resolution and flexibility (Fig. 5B). To make radiographically visible objects, gold was incorporated in the stents postprinting, rendering them radiopaque (fig. S11A). When compared to the native stents, the gold-labeled stents showed slightly improved mechanical properties (fig. S11B) because of the presence of metal particles (44), while preserving cytocompatibility (fig. S11C). After cleaning and drying, the stents were loaded into a customized delivery device (Fig. 5, C and D, and movie S1) developed for precise stent placement in a rabbit's trachea at the level of the third cervical (C3) vertebrae. The delivery device was inserted in the anesthetized rabbit through a 5.5-mm uncuffed endotracheal tube, and the stent was deployed at the targeted position. After the placement, the position and the integrity of the stent were reviewed by flexible tracheoscopy (Fig. 5E) and radiography (Fig. 5F).

Six animals allocated in three groups were monitored for 2, 6, and 10 weeks, respectively, to assess the in vivo biocompatibility and bioresorbability of the printed stents. Allocation of the rabbits in the groups and the corresponding types of stents they received are reported in table S1. Radiographs showed that the stents stayed unchanged at the insertion place in five of six animals and were visible

up to 7 weeks after the placement (Fig. 5F and fig. S12). Only in one animal, the stent migrated cranially to the C2 vertebrae after week 3 (fig. S12B), probably due to sneezing. During the first week, all rabbits showed intermittent stridor at exertion. They also exhibited periodic sneezing without nasal discharge between weeks 3 and 4 that was reduced in two of three animals after the treatment with acetylcysteine (3 mg/kg, p.o.). At euthanasia of the animals with the observation period of 2 and 6 weeks, macroscopic examination revealed the intact stents at the place of the insertion. After 10 weeks, the lungs of both animals upon euthanasia were clean and neither the stents nor pieces of stents could be recovered.

In addition to macroscopic examination, biocompatibility evaluation (45) based on histological findings at the contact surface between the stent and the mucosa showed a clear trend of inflammation and tissue response between different groups of animals (Fig. 5, G to I). When compared to the distal area, the stented area presented a slight overall reaction after 2 weeks that progressed and peaked at week 6 and became minimal or undetectable after 10 weeks (table S1). Similar to previously reported studies on airway stents (36, 37, 39), severe acute inflammation with infiltration of heterophils and mild to moderate dilatation and hyperemia was observed in animals after 2 weeks in the stented area (Fig. 5G). This remained on a similar level up to week 6 in the stented area (Fig. 5H), while declining in the distal area. As expected, chronic inflammation developed at week 6 with abundant lymphocytes, including plasma cells and macrophages (Fig. 5H). Eosinophils were noticeable in a small number up to 6 weeks. As shown in Fig. 5 (G to I), thin and thick irregular epithelia with ulcerations and necrosis were present up to week 6. Epithelial squamous metaplasia was present focally in most of the animals up to 6 weeks, with multifocal changes in one animal of 6 weeks of survival time (Fig. 5H). At week 10 (Fig. 5I), we found tracheal tissue of normal morphology with ciliated columnar epithelium without any traces of inflammation. The stent design (round versus slightly flattened) had no impact on inflammation and tissue response.

### DISCUSSION

It is of prime importance that the bioresorbable stents maintain their mechanical properties during the treatment, especially at the early stage after the insertion. In vitro, dry and wet stents showed approximately the same dimensions and mechanical behavior up to 12 weeks (Fig. 4, F, I and J). This is an important requirement for a functional stent since wet conditions are more representative of the real application conditions. Furthermore, unchanged dimensions of the stents (Fig. 4, G and H, and fig. S10) when compressive resistance decreases for ca. 50% (Fig. 4D) should keep them in place despite the decrease in mechanical properties. In vivo, the gold-loaded stents based on the optimal dual-polymer resin of high- and low-MW poly(DLLA-co-CL) methacrylate in weight ratio of 75/25 preserved sufficient mechanical force to generally stay at the place of the insertion for 7 weeks. Afterward, they were not radiographically visible and at week 10, they were not present in the respiratory tract. In vitro, the evolution of mass loss of the printed objects (Fig. 4B) indicated bulk degradation with autocatalytic effect as the degradation mode (46). These materials lose their mechanical properties faster than their mass (Fig. 4, B and D), as the ester bond cleavage is ongoing from the beginning of the degradation process, while the diffusion of the monomers and oligomers resulting from the degradation of the

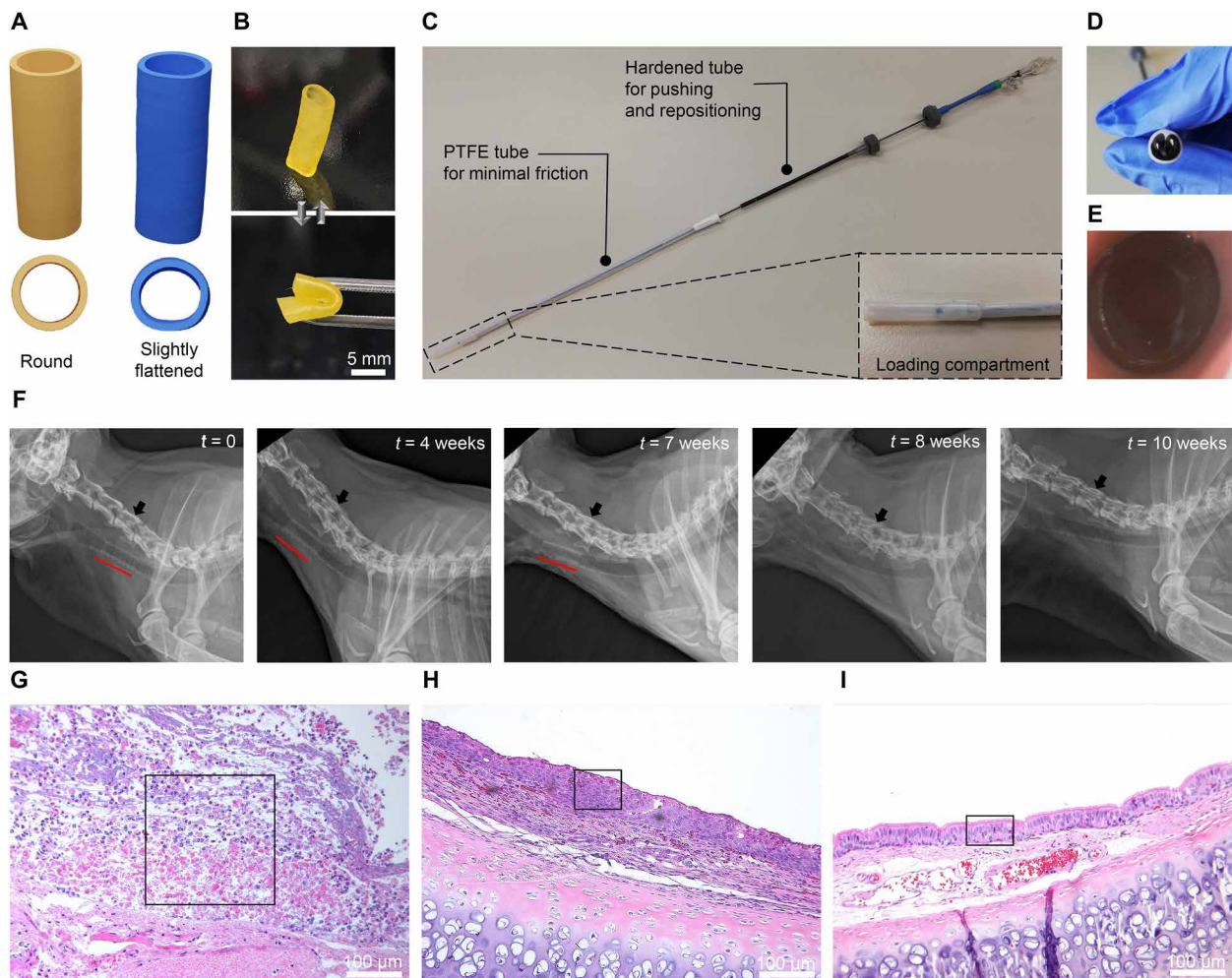


**Fig. 5. In vivo evaluation of radiopaque customized 3D printed stents based on 75/25 (w/w) P1/P2 dual-polymer resin with 1 wt % gold incorporated postprinting in healthy rabbits.** (A) 3D printing files (.stl) of round (yellow) and slightly flattened (blue) stents. (B) Highly flexible 3D printed animal-tailored airway stents. (C) Customized delivery device used to insert the stent in the trachea. Inset: Compartment for loading the stent. (D) Stent loaded in the delivery device before insertion. (E) Tracheoscopy image of an intact stent in the rabbit's trachea in the area of C3 vertebrae after the insertion. (F) Radiographs of a rabbit with the observation period of 10 weeks. Position of the stent is marked with a red line. Black arrows indicate the C4 vertebrae. (G to I) Inflammatory and tissue morphology changes in the rabbit's trachea 2 (G), 6 (H), and 10 weeks (I) after the stent insertion. Black rectangles represent the parts of the main morphological changes over time including the area of inflammation and necrosis (G), squamous metaplastic epithelium (H), and pseudostratified columnar (respiratory) epithelium (I). Hematoxylin and eosin staining, magnification of  $10 \times 10$ . Photo credits: Yinyin Bao, ETH Zurich (B); Nevena Paunović, ETH Zurich (C and D); and Anna Karoline Geks, University of Zurich (E).

polymer matrix is a relatively slow process (47, 48). On the basis of the literature (47), the same profile of degradation, but with higher degradation rate, is expected in vivo, particularly due to enzymatic activity and mechanical stress. The slower degradation observed in vitro compared to in vivo might also come from the design of the degradation test, which was focused on human application. In accordance to the thickness of a typical silicone airway stent used in human medicine, the in vitro tests were performed on 1-mm-thick stents at  $37^{\circ}\text{C}$  and pH 7.4. The thickness of the stents used in the animal study had to be decreased to 0.6 mm to achieve the required pliability for the insertion, thus making them more susceptible toward degradation. In addition, rabbits have higher body temperature (ca.  $39.5^{\circ}\text{C}$ ) (49), which increases the rate of hydrolysis of polymer ester bonds. In the accelerated in vitro degradation experiment conducted at  $50^{\circ}\text{C}$ , the stents decreased their mechanical properties gradually with the hydrolysis of ester bonds (Fig. 4E). Once the

mass of the stents dropped below 60% of the initial mass (Fig. 4B), the mechanical stability of the stents was too low and even a slight compression could break them. By that moment, the polymer scaffold became less hydrophobic due to hydroxyl and carboxyl groups formed upon hydrolysis, which together with accumulation of hydrophilic monomers and oligomers entrapped deep in the polymer network caused high water uptake (Fig. 4C) and led to a material with a hydrogel structure (Fig. 4, K and L). While this will eventually result in complete disintegration of the stent in the trachea, the structure will likely be fragmented to very soft pieces that could be easily resorbed or moved toward larynges and further ingested. This hypothesis was supported in vivo by the presence of intact stents in extracted rabbits' tracheas at weeks 2 and 6, as well as by the absence of stents and fragments of stents 10 weeks after the insertion.

The elastic cross-linked stents we developed and assessed in the in vivo study showed superior performance compared to previously



reported bioresorbable stents made from thermoplastic polymers such as poly( $\epsilon$ -caprolactone), which are prone to stress relaxation or even permanent deformation when being constrained before implantation (18). Our dual-polymer stents were highly flexible, elastic, and restored their size and shape immediately after the deployment. The inflammation pattern that peaked at week 6 postinsertion was similar to the reaction described in previous reports on bioresorbable airway stents (36, 37). Besides, epithelial ulcerations with chronic lymphocytic inflammation were reported underneath all types of airway stents used in rabbit models, including metallic, silicone, and biodegradable poly(L-lactide) materials (39). On a tissue level, the mechanical stress applied by the stent on the healthy trachea caused transformation from pseudostratified columnar epithelium to squamous metaplastic epithelium. Similar effects, which may end up in obstructive granulation tissue formation, are also typically observed in humans (50). We intentionally chose the material with the stronger resistance to uniaxial compression at high displacement in a compression test (Fig. 2D), compared to a silicone stent, to maximize the mechanical performance and assure that the stent would stay in place and keep the tracheal lumen open during the initial several weeks of the treatment. Despite the high local stresses expected from this stiffer stent, all histological changes were completely reversible after the stent disappeared, confirming the biocompatibility of the produced medical device. Future studies should aim at the minimization of the trauma related to the stent insertion to allow for the use of these stents in disease models reproducing obstructed airways.

In summary, we developed a series of biomedical inks based on blends of poly(DLLA-co-CL) methacrylates with diverse polymer chain length and geometry that can serve to DLP 3D print biocompatible elastic materials with tunable mechanical properties and predictable degradation. The key advancement in terms of ink design lies in the combination of high- and low-MW photopolymers in the same resin. This resulted in 3D printed objects that combine the enhanced strength arising from high cross-linking density and high elasticity provided by long and flexible polymer chains. Printing at higher temperatures with our customized heating system and the addition of a low-MW polymer in the resin reduced viscosity and enabled the generation of objects with complex architecture at high resolution and surface quality. These inks allowed for the manufacturing of customized prototype bioresorbable airway stents with mechanical properties comparable to state-of-the-art silicone stents. FE modeling was conducted to provide design guidelines for choosing the optimal thickness for the defined radius and normal stiffness of the stent for an individual patient. After further optimization, the proposed airway stents might be used to treat patients suffering from CAO in a more personalized way. These stents would disappear over time, preventing the need of additional interventions, which is particularly important for children and elderly patients. While the biomedical inks described in this study were primarily conceived to 3D print airways stents, the tunable mechanical properties of the produced elastic objects, as well as their biodegradable feature, could also be exploited in the future to design other types of personalized stents and medical devices.

## MATERIALS AND METHODS

### Materials

Pentaerythritol, methacryloyl chloride, triethylamine, tetrahydrofuran (THF; extra dry), and acetone (extra dry) were purchased from

Acros Organics. CL was obtained from Tokyo Chemical Industry. 3,6-Dimethyl-1,4-dioxane-2,5-dione (DLLA) was purchased from Huizhou Foryou Medical Devices Co. Ltd. or Acros Organics. Tin(II)-2-ethylhexanoate [Sn(Oct)<sub>2</sub>], 2,2-diethyl-1,3-propanediol, sodium bicarbonate (NaHCO<sub>3</sub>), sodium chloride (NaCl), (+)- $\alpha$ -tocopherol (vitamin E), NVP, BAPO, 1-(phenyldiazenyl)naphthalen-2-ol (Sudan I), borane-*tert*-butylamine complex [(CH<sub>3</sub>)<sub>3</sub>CNH<sub>2</sub>·BH<sub>3</sub>], and lithium bromide (LiBr) were purchased from Sigma-Aldrich. Hydrogen tetrachloroaurate(III) trihydrate (HAuCl<sub>4</sub>) was obtained from abcr. Hexane, dichloromethane (DCM), and dimethylformamide (DMF) were purchased from Thermo Fisher Scientific. Dimethyl sulfoxide-d<sub>6</sub> (DMSO-d<sub>6</sub>) was obtained from ReseaChem. Methanol and 2-propanol were provided by VWR Chemicals. Midazolam was purchased from Sintetica. Alfaxalon was purchased from Jurox UK. Isoflurane was purchased from Provet AG. PBS was obtained from Thermo Fisher Scientific. All chemicals were used as received.

### Polymer synthesis

Poly(DLLA-co-CL)s were synthesized by ring-opening polymerization of DLLA and CL initiated by pentaerythritol (four-arm structure) or 2,2-diethyl-1,3-propanediol (linear structure), with Sn(Oct)<sub>2</sub> as a catalyst (fig. S1) (26). The MW of the polymers was controlled by varying the molar feed ratio of the monomers and initiators ([M]/[I]). Thereafter, poly(DLLA-co-CL)s were functionalized with methacryloyl chloride in the presence of triethylamine in THF (fig. S1) (26).

Representative synthesis of **P1** (four-arm)—pentaerythritol (0.19 g, 1.4 mmol), CL (13.60 g, 120 mmol), DLLA (7.48 g, 52 mmol), and Sn(Oct)<sub>2</sub> (5  $\mu$ l, 0.015 mmol)—were added to a Schlenk flask. The flask was exposed to vacuum for 1 hour and purged with argon for three cycles to remove water and oxygen and then placed in an oil bath at 140°C for 48 hours under stirring. The product was dissolved in THF and precipitated in hexane, resulting in a transparent and highly viscous polymer. On the basis of <sup>1</sup>H nuclear magnetic resonance (<sup>1</sup>H NMR) spectroscopy, the conversions of DLLA and CL were ca. 90 and 99%, respectively (fig. S13). The synthesis resulted in a polymer of low polydispersity, which was confirmed by size exclusion chromatography (SEC) (fig. S14 and table S2). The unfunctionalized polymer (18.71 g) was then dissolved in THF (100 ml). After the addition of triethylamine (2.34 ml, 16.8 mmol), the solution was purged with nitrogen for 15 min. Methacryloyl chloride (1.63 ml, 16.8 mmol) was diluted in THF (5 ml) and added dropwise to the polymer solution while stirring and cooling in an ice bath. The reaction mixture was then stirred for 24 hours at room temperature. Afterward, the salts were removed by centrifugation (4000g, 4°C, 20 min) and vitamin E (0.05 g) was added to the supernatant to prevent premature cross-linking. The supernatant was concentrated under vacuum, followed by precipitation in methanol. The obtained transparent viscous polymer was dried under high vacuum for a week. On the basis of <sup>1</sup>H NMR spectroscopy, the conversion of hydroxyl end groups of the polymer chains was 70 to 87% (fig. S15). The same procedure was followed for the synthesis of four-arm polymers of MW 5000 to 11,000 g mol<sup>-1</sup>, CL/DLLA molar ratio of 7/3, with varying [M]/[I] (figs. S13 to S15 and table S2).

Representative synthesis of **P2** (linear)—2,2-diethyl-1,3-propanediol (6.61 g, 50 mmol), CL (11.38 g, 100 mmol), DLLA (14.23 g, 100 mmol), and Sn(Oct)<sub>2</sub> (160  $\mu$ l, 0.5 mmol)—were added to a Schlenk flask. The synthesis was further performed following the same protocol as described for unfunctionalized **P1** polymer. The conversions of DLLA and CL based on <sup>1</sup>H NMR spectroscopy were ca. 55 and 99%,

respectively (fig. S16A). The synthesis resulted in a polymer of low polydispersity, which was confirmed by matrix-assisted laser desorption/ionization–time-of-flight (MALDI-TOF) (fig. S17). The unfunctionalized polymer (18 g) was dissolved in THF (150 ml). After the addition of triethylamine (17.0 ml, 122 mmol), the solution was purged with nitrogen for 15 min. Methacryloyl chloride (11.0 ml, 114 mmol) was diluted in THF (10 ml) and added dropwise to the polymer solution while stirring and cooling in an ice bath. The reaction mixture was stirred for 24 hours at room temperature. Afterward, the salts were removed by centrifugation (4000g, 4°C, 20 min) and the supernatant with vitamin E (0.05 g) was concentrated. The polymer was dissolved in DCM (200 ml), washed with saturated NaHCO<sub>3</sub> and NaCl aqueous solutions, and dried with anhydrous Na<sub>2</sub>SO<sub>4</sub>. After addition of vitamin E (0.05 g), the solution was concentrated under vacuum and the polymer was further dried under high vacuum for a week. On the basis of <sup>1</sup>H NMR, the conversion of hydroxyl end groups of the polymer chains was 51 to 54% (fig. S16B). The same procedure was followed for the synthesis of four-arm polymer of MW 1200 g mol<sup>-1</sup>, CL/DLLA molar ratio of 7/3, with pentaerythritol as initiator and with varying [M]/[I], while polydispersity was quantified by SEC (figs. S13 to S15 and table S2).

### Polymer characterization

<sup>1</sup>H NMR spectra were recorded on Bruker AV400 spectrometer at 400 Hz using DMSO-d<sub>6</sub> as a solvent. SEC was carried out on a Viscotek TDAmass system equipped with two Viscotek columns [D3000, poly(styrene-co-divinylbenzene)] and differential refractive index detector (TDA 302, Viscotek). All samples were dissolved in DMF, filtered using 0.2-μm syringe filters (polytetrafluoroethylene, PTFE) and eluted using DMF with LiBr (0.1 wt %) as a mobile phase (mobile phase flow, 0.5 ml min<sup>-1</sup>). The macromolecular characteristics were determined relative to a poly(methyl methacrylate) standard curve (PSS Polymer Mainz; 2500 to 89,300 g mol<sup>-1</sup>). Differential scanning calorimetry (DSC) analysis was performed using TA Q200 DSC (TA Instruments–Waters LLC). The samples (ca. 10 mg) were placed on Tzero hermetic pans (TA Instruments–Waters LLC) and exposed to heat-cool-heat cycles from -80°C to 200°C under nitrogen flow (50 ml min<sup>-1</sup>) using heating and cooling rates of 10°C min<sup>-1</sup>. Data were analyzed using TA Instruments Universal Analysis 2000 software (5.5.3). Viscosity measurements were performed using a HAAKE RheoStress 600 rotational rheometer (Thermo Electron Corporation) with cone and plate geometry (35 mm/2°). Viscosity was determined at a shear rate of 100 s<sup>-1</sup> in the temperature range of 70 to 100°C, applying a heating rate of 0.05°C s<sup>-1</sup>. Data were analyzed by RheoWin Data Manager (Thermo Electron Corporation). Fourier transform infrared spectra were recorded on a Perkin-Elmer Spectrum 65 (Perkin-Elmer Corporation) in transmission mode in the range of 600 to 4000 cm<sup>-1</sup>. MALDI-TOF spectra were measured on a Bruker Daltonics Ultraflex II spectrometer in the positive ion reflector mode using trans-2-[3-(4-tert-butylphenyl)-2-methyl-2-propenylidene] as a matrix.

### DLP 3D printing

Resins were prepared by adding a solution of BAPO (photoinitiator, 1.0 wt %) and Sudan I (blue light-absorbing dye used to reduce the curing depth, 0.03 wt %) in NVP (8.0 wt %) to the photopolymers and vitamin E (radical inhibitor used to prevent premature cross-linking, 0.3 wt %). The resins were sonicated at 60°C until a homogeneous mixture was obtained. A commercial DLP 3D printer (Asiga

PICO2) comprising the light-emitting diode light source of 405 nm with customized resin tray and printing head with heating functions (fig. S4) was used to fabricate all the objects. The printing was performed at a temperature of 80°C, with exposure time of 3.3 s, and initial exposure time of 15 s. After printing, the printed objects were cleaned in acetone and 2-propanol and then cured in an Asiga Pico Flash UV chamber for 15 min.

### Mechanical characterization of 3D printed objects

Tensile, compression, and Mylar loop tests were performed using an AGS-X (Shimadzu) universal testing machine with a 100-N capacity load cell. Tensile tests were carried out on dog bone-shaped 3D printed specimens (ASTM 638 type IV) with a gauge length of 13 mm at a rate of 20 mm min<sup>-1</sup>. Compression tests were performed on nonmeshed tubular 3D printed specimens (*H* of 10.0 mm,  $\Phi$  of 16.0 or 8.0 mm, and thickness of 1.0 or 1.2 mm) at a rate of 10 mm min<sup>-1</sup>. Every sample was tested three times. Mylar loop experiments were carried out on tubular 3D printed specimens (*H* of 10.0 mm,  $\Phi$  of 16.0 mm, and thickness of 1.2 mm), with an in-house-developed Mylar loop (fig. S9) at a rate of 20 mm min<sup>-1</sup>. Every sample was tested three times. True stress and strain were calculated using Eqs. 1 and 2 (51), respectively

$$\sigma = \frac{F}{A_0} \times \left(1 + \frac{L}{L_0}\right) \quad (1)$$

$$\epsilon = \ln\left(1 + \frac{L}{L_0}\right) \quad (2)$$

where  $\sigma$  is true stress,  $\epsilon$  is the true strain,  $F$  is the force,  $A_0$  is the initial cross-sectional area,  $L$  is the elongation, and  $L_0$  is the initial gauge length. Normal stiffness was calculated as a slope of the initial linear region of compression-displacement curves obtained in uniaxial compression tests.

### Numerical simulations

The simulations were carried out using the commercial nonlinear FE package ABAQUS 2017 (SIMULIA). The ABAQUS/STANDARD solver was used for all simulations. To describe the material properties of our polymers, given the softening-hardening nature of stress-strain curves, we assumed an incompressible Gent hyperelastic material model (52) and used MATLAB curve fitting tool to fit the full range of dog bone-shaped tensile test specimens to this model. The obtained parameters (shear modulus and stretch limit) are introduced to simulations using a user-defined subroutine (\*UHYPER subroutine in ABAQUS). The tubes are discretized with solid elements (type C4D8) and compressed between two rigid plates that are meshed with shell elements (type S4). We performed dynamic implicit analysis (\*DYNAMIC module in ABAQUS) by lowering the plate until it touches the tube and compressing it to the desired deformation against the bottom fixed plate. A simple contact law was assigned to the model with a hard contact for normal behavior and a frictionless tangential behavior between the rigid plates and the tube. The reaction force of the top plate was recorded as a function of the applied displacement in the normal direction and was compared against experimental compression test data. Last, a Python script was developed to perform a parametric study on the role of variation in radius and thickness on the normal stiffness of tubes. The slope of the initial linear region of the compression-displacement curve is reported as the normal stiffness of the tubes.

### In vitro degradation study

The 3D printed nonmeshed tubular specimens ( $H$  of 10.0 mm,  $\varnothing$  of 8.0 mm, and thickness of 1.0 mm) were immersed separately in 50 ml of PBS (pH 7.4) at 37° or 50°C, in tightly closed 50-ml Falcon tubes. The buffer was replaced at weekly intervals. At each sampling time point, the specimens were taken out, rinsed with deionized water, wiped with paper tissue, and dried under vacuum at 50°C overnight. The water uptake (wt %) was calculated using Eq. 3

$$\text{water uptake} = \frac{\text{wt}_{\text{wet}} - \text{wt}_{\text{dry}}}{\text{wt}_{\text{dry}}} \times 100 \quad (3)$$

where  $\text{wt}_{\text{wet}}$  is the mass of a stent in a wet state after the wiping, and  $\text{wt}_{\text{dry}}$  is the mass of a stent in a dry state after drying under vacuum. The dried specimens were studied by a uniaxial compression test. In the degradation study performed at 37°C, a compression test was also performed with stents in a wet state. Both degradation studies were performed with four 3D printed tubular specimens but with two different batches of **P1** and **P2**. Objects were visualized using a Keyence scanning laser microscope.

### Cell culture

Human lung epithelial cells (A549, American Type Culture Collection) were cultured at 37°C in a humidified atmosphere with 5% CO<sub>2</sub>. The cells were used up to passage number 12 and were tested for mycoplasma contamination (MycAlert Mycoplasma Detection Kit, Lonza) at first and last passage numbers. A549 cell line was cultured in complete medium containing DMEM (Dulbecco's modified Eagle's medium) (high glucose, GlutaMax, pyruvate; Thermo Fisher Scientific) supplemented with 10% fetal bovine serum (Thermo Fisher Scientific) and 1% penicillin-streptomycin (Thermo Fisher Scientific).

### In vitro cytocompatibility test

The tests were performed in 24-well plates with seeding density of 50,000 cells per well and repeated in three independent experiments, each one with three-well replicates. For positive and negative controls, cells were incubated in complete medium with 10 mM hydrogen peroxide and complete medium only, respectively, under the same conditions as the tested materials. Cell viability was determined using the MTS assay (CellTiter 96 Aqueous One Solution Cell Proliferation Assay, G3580, Promega) according to the manufacturer's instructions and was calculated as a percentage of the negative control. 3D printed disks (native or loaded with gold, see the "Manufacturing radiopaque stents" section) were washed in acetone (50 ml) for 30 min, dried, and then washed in PBS (50 ml, pH 7.4) overnight. Afterward, the objects were dried under vacuum at room temperature for 24 hours and then cured in an Asiga Pico Flash UV chamber for 20 min. The disks were presoaked in 10 ml of medium for 20 min before the incubation.

Tests based on extracts are as follows: The testing procedure was adapted from international standards (ISO) for biological evaluation of medical devices, tests for in vitro cytotoxicity (ISO 10993-5:2009), and sample preparation and reference materials (ISO 10993-12:2009) (34, 35). In particular, 3D printed disks ( $H$  of 0.8 mm and  $\varnothing$  of 22 mm) were incubated in a six-well plate with 2.8 ml of medium per disk (ca. 2.7 cm<sup>2</sup>/ml) at 37 ± 1°C in a humidified atmosphere with 5% CO<sub>2</sub> for 72 ± 2 hours. After 24 hours of cell seeding, the medium was removed and replaced with extracts and controls. Afterward, the plate was incubated for additional 24 ± 1 hours. Test

based on Transwell inserts is as follows: Immediately after cell seeding, Transwell permeable supports (ThinCert Cell Culture Inserts 24 well, sterile, translucent, pore size of 8 μm; Greiner Bio-One) were placed in corresponding wells. 3D printed disks ( $H$  of 0.8 mm and  $\varnothing$  of 5.5 mm) were placed on top of the inserts and covered with medium (100 μl). The plate was incubated for 48 ± 1 hour.

### Manufacturing radiopaque stents

To make radiographically visible objects, gold was incorporated in the structure after printing. The stents were soaked in an acetone solution of HAuCl<sub>4</sub> (10 mg ml<sup>-1</sup>) for 30 min at room temperature upon 3D printing. After washing with acetone and drying, they were soaked in an acetone solution of (CH<sub>3</sub>)<sub>3</sub>CNH<sub>2</sub> BH<sub>3</sub> (20 mg ml<sup>-1</sup>) to reduce gold ions to elemental gold. The stents were again washed in acetone, dried, and cured for 15 min in an Asiga Pico Flash UV chamber. Thereafter, they were cleaned in acetone (50 ml) for 30 min, dried, washed in PBS (50 ml, pH 7.4) for 24 hours, rinsed with deionized water, and then dried in a desiccator for 24 hours.

### Fabrication of the delivery device

In-house delivery device was composed of two coaxial tube assemblies (Fig. 5C). The outer tube was fabricated from PTFE to minimize friction during insertion. Using a heat-shrinking process, the tube was flared at one end to create a compartment for loading a crimped stent. The inner tube was a modified Acclarent balloon dilation device (Acclarent, Inspira Air; 7 × 24 mm) modified using a Pebax heat-shrink tubing to increase stiffness and decrease balloon size. This part was used for pushing the stent out of the device and repositioning if necessary. The device was applied through a commercial 5.5-mm ID (inside diameter) uncuffed endotracheal tube (5.5-mm ID; Shiley Oral/Nasal Endotracheal Tubes, Cuffless, Non-DEHP, Murphy Eye). As the procedure of stent insertion lasts only for a few seconds, no oxygen supply was needed.

### Design of the stents for in vivo study

A CT scan of the head and lungs was acquired for each rabbit. The DICOM (Digital Imaging and Communications in Medicine) file was imported into the open-source InVesalius software (version 3.1). The area of interest, i.e., the larynx and the trachea up to the first bronchial branch, was cropped and then isolated using a watershed threshold between -1024 and -700 Hounsfield units. The isolated tracheal surface was then exported as an stereolithography (STL) mesh. The mesh for each animal was imported into the CAM package Rhino 3D (version 6, McNeel Software), and all were reoriented such that the bottom of larynx lays on the  $xy$  plane and the trachea was oriented as vertically as possible along the  $z$  axis. A series of 16 planes offset from 30 to 46 mm below the  $xy$  plane were created and then intersected with the mesh. The result was a series of planar curves equating to the outline of the trachea for each animal (within the area of interest). The length of each curve was measured and corresponding curves at each tracheal position across the six animals were averaged. The series of averaged lengths were used as the circumference for a group of coaxial circles, each spaced 1 mm apart. These circles were converted to a nonuniform tubular surface using the Rhino 3D "Loft" command. Last, a second surface was created by offsetting inward by the desired stent wall thickness of 0.6 mm. The two surfaces were joined, capped, and exported as a printable STL mesh.

**In vivo study**

The experimental protocol was approved by the Zürich Cantonal Animal Ethics Committee (ZH069/18) and performed according to the Swiss Animal Welfare Act (TSchG, 455). The stents were inserted in nine adult female New Zealand white rabbits (Charles River Laboratories, Germany) with age of 6 months and average weight of 3.5 kg. Before anesthesia, animals were preoxygenated with oxygen (2 liter min<sup>-1</sup>) over 5 min through a breathing mask. Anesthesia was induced by intranasal application of midazolam (0.1 mg kg<sup>-1</sup>) and alfaxalone (3.0 to 5.0 mg kg<sup>-1</sup>). After intravenous application of a bolus of propofol (0.6 mg kg<sup>-1</sup>), a bronchoscope (Ambu aScope 4 Broncho slim 3.8/1.2) was introduced into the trachea and the endotracheal tube slid over the endoscope to secure the airway. The anesthesia was maintained by isoflurane and oxygen. The delivery device for the stent was lubricated with a methylcellulose-based lubricant and the stent was crimped and loaded in. It was applied through an endotracheal tube, and the stent was positioned in the area of the C3 vertebrae. After the placement, the position and the integrity of the stent were reviewed by flexible tracheoscopy (Ambu aScope 4 Broncho Regular 3.8/1.2) and radiographic examination (in lateral recumbency of the animal). Three animals were excluded from the analysis because of *Aspergillus* infection, deep stent insertion, and respiratory distress in the absence of the stent. The remaining six animals were allocated into three groups of two according to the monitoring time (2, 6, and 10 weeks). The animals were housed in groups in stables with free access to hay and water. They were checked daily for respiratory distress, food, and water intake, while radiographic examinations were performed once per week. Body weight was checked 24 hours before surgery and frequently during the postoperative observation period.

The animals were euthanized at 2, 6, or 10 weeks after stent placement. Complete histopathological examination was performed from the trachea including the stented and the area distally to the stent, which was harvested and preserved in 4% formalin. Samples were dehydrated, embedded in paraffin, cut in 2- to 4- $\mu$ m-thick sections and further stained with hematoxylin and eosin to describe the overall structure and inflammation and van Gieson–Elastica for presence and matrix deposition (collagen and elastin). Additional immunohistological stainings were performed with  $\alpha$ -smooth muscle actin for matrix producing fibroblasts/myofibroblasts and with cyclooxygenase 2 and inducible nitric oxide synthase, representing the inflammatory markers. The stained sections were semiquantitatively evaluated using microscopy (Leica DMR System with Leica DFC 320 camera, Leica Microsystems) by two observers blinded to the experimental groups. The scoring system for evaluation of differences between the treated and nontreated tracheal tissue was based on inflammatory and tissue reactions, including epithelial and vascular changes, with remodeling within the tracheal wall, and it was further used for semiquantitative analysis.

**Statistical analysis**

Statistical significance in cytotoxicity experiments between the treated groups and a negative control was calculated by one-way analysis of variance (ANOVA) with Tukey's comparison test with *P* value < 0.001 considered as significant.

**SUPPLEMENTARY MATERIALS**

Supplementary material for this article is available at <http://advances.sciencemag.org/cgi/content/full/7/6/eabe9499/DC1>

**REFERENCES AND NOTES**

1. A. Ernst, D. Feller-Kopman, H. D. Becker, A. C. Mehta, Central airway obstruction. *Am. J. Respir. Crit. Care Med.* **169**, 1278–1297 (2004).
2. C. P. Wild, E. Weiderpass, B. W. Stewart, *World cancer report: Cancer Research for Cancer Prevention* (International Agency for Research on Cancer, Lyon, France, 2020).
3. P. Lee, E. Kupeli, A. C. Mehta, Airway stents. *Clin. Chest Med.* **31**, 141–150 (2010).
4. Y. Saito, H. Imamura, Airway stenting. *Surg. Today* **35**, 265–270 (2005).
5. L. Freitag, M. Gordes, P. Zarogoulidis, K. Darwiche, D. Franzen, F. Funke, W. Hohenforst-Schmidt, H. Dutau, Towards individualized tracheobronchial stents: Technical, practical and legal considerations. *Respiration* **94**, 442–456 (2017).
6. S. C. Ligon, R. Liska, J. Stampfl, M. Gurr, R. Mülhaupt, Polymers for 3D printing and customized additive manufacturing. *Chem. Rev.* **117**, 10212–10290 (2017).
7. B. Grigoryan, S. J. Paulsen, D. C. Corbett, D. W. Sazer, C. L. Fortin, A. J. Zaita, P. T. Greenfield, N. J. Calafat, J. P. Gounley, A. H. Ta, F. Johansson, A. Randles, J. E. Rosenkrantz, J. D. Louis-Rosenberg, P. A. Galie, K. R. Stevens, J. S. Miller, Multivascular networks and functional intravascular topologies within biocompatible hydrogels. *Science* **364**, 458–464 (2019).
8. X. Liu, H. Yuk, S. Lin, G. A. Parada, T.-C. Tang, E. Tham, C. de la Fuente-Nunez, T. K. Lu, X. Zhao, 3D printing of living responsive materials and devices. *Adv. Mater.* **30**, 1704821 (2018).
9. J. U. Lind, T. A. Busbee, A. D. Valentine, F. S. Pasqualini, H. Yuan, M. Yadid, S.-J. Park, A. Kotikian, A. P. Nesmith, P. H. Campbell, J. J. Vlassak, J. A. Lewis, K. K. Parker, Instrumented cardiac microphysiological devices via multi-material 3D printing. *Nat. Mater.* **16**, 303–308 (2017).
10. R. S. H. Smith, C. Bader, S. Sharma, D. Kolb, T.-C. Tang, A. Hosny, F. Moser, J. C. Weaver, C. A. Voigt, N. Oxman, Hybrid living materials: Digital design and fabrication of 3D multimaterial structures with programmable biohybrid surfaces. *Adv. Funct. Mater.* **30**, 1907401 (2020).
11. M. Rafiee, R. D. Farahani, D. Theriault, Multi-material 3D and 4D printing: A survey. *Adv. Sci.* **7**, 1902307 (2020).
12. T.-Y. Huang, M. S. Sakar, A. Mao, A. J. Petruska, F. Qiu, X.-B. Chen, S. Kennedy, D. Mooney, B. J. Nelson, 3D printed microtransporters: Compound micromachines for spatiotemporally controlled delivery of therapeutic agents. *Adv. Mater.* **27**, 6644–6650 (2015).
13. B. C. Pereira, A. Isreb, M. Isreb, R. T. Forbes, E. F. Oga, M. A. Alhnan, Additive manufacturing of a point-of-care “polypill”: Fabrication of concept capsules of complex geometry with bespoke release against cardiovascular disease. *Adv. Healthc. Mater.* **9**, 2000236 (2020).
14. G. L. Koons, M. Diba, A. G. Mikos, Materials design for bone-tissue engineering. *Nat. Rev. Mater.* **5**, 584–603 (2020).
15. K. Liang, D. Brambilla, J.-C. Leroux, Is 3D printing of pharmaceuticals a disruptor or enabler? *Adv. Mater.* **31**, 1805680 (2019).
16. D. A. Zopf, S. J. Hollister, M. E. Nelson, R. G. Ohye, G. E. Green, Bioresorbable airway splint created with a three-dimensional printer. *N. Engl. J. Med.* **368**, 2043–2045 (2013).
17. K. Liang, S. Carmone, D. Brambilla, J.-C. Leroux, 3D printing of a wearable personalized oral delivery device: A first-in-human study. *Sci. Adv.* **4**, eaat2544 (2018).
18. F. Rezgui, M. Swistek, J. M. Hiver, C. G'Sell, T. Sadoun, Deformation and damage upon stretching of degradable polymers (PLA and PCL). *Polymer* **46**, 7370–7385 (2005).
19. C. Yu, J. Schimelman, P. Wang, K. L. Miller, X. Ma, S. You, J. Guan, B. Sun, W. Zhu, S. Chen, Photopolymerizable biomaterials and light-based 3D printing strategies for biomedical applications. *Chem. Rev.* **120**, 10695–10743 (2020).
20. D. K. Patel, A. H. Sakhaei, M. Layani, B. Zhang, Q. Ge, S. Magdassi, Highly stretchable and UV curable elastomers for digital light processing based 3D printing. *Adv. Mater.* **29**, 1606000 (2017).
21. Y. Luo, G. Le Fer, D. Dean, M. L. Becker, 3D printing of poly(propylene fumarate) oligomers: Evaluation of resin viscosity, printing characteristics and mechanical properties. *Biomacromolecules* **20**, 1699–1708 (2019).
22. N. Bhattacharjee, C. Parra-Cabrera, Y. T. Kim, A. P. Kuo, A. Folch, Desktop-stereolithography 3D-printing of a poly(dimethylsiloxane)-based material with Sylgard-184 properties. *Adv. Mater.* **30**, 1800001 (2018).
23. F. P. W. Melchels, J. Feijen, D. W. Grijpma, A review on stereolithography and its applications in biomedical engineering. *Biomaterials* **31**, 6121–6130 (2010).
24. F. P. W. Melchels, J. Feijen, D. W. Grijpma, A poly(D,L-lactide) resin for the preparation of tissue engineering scaffolds by stereolithography. *Biomaterials* **30**, 3801–3809 (2009).
25. M. Zarek, M. Layani, I. Cooperstein, E. Sacyani, D. Cohn, S. Magdassi, 3D printing of shape memory polymers for flexible electronic devices. *Adv. Mater.* **28**, 4449–4454 (2016).
26. B. G. Amsden, G. Misra, F. Gu, H. M. Younes, Synthesis and characterization of a photo-cross-linked biodegradable elastomer. *Biomacromolecules* **5**, 2479–2486 (2004).
27. L. Elomaa, S. Teixeira, R. Hakala, H. Korhonen, D. W. Grijpma, J. V. Seppälä, Preparation of poly( $\epsilon$ -caprolactone)-based tissue engineering scaffolds by stereolithography. *Acta Biomater.* **7**, 3850–3856 (2011).
28. G. Le Fer, Y. Luo, M. L. Becker, Poly(propylene fumarate) stars, using architecture to reduce the viscosity of 3D printable resins. *Polym. Chem.* **10**, 4655–4664 (2019).

29. A. Helminen, H. Korhonen, J. V. Seppälä, Biodegradable crosslinked polymers based on triethoxysilane terminated polylactide oligomers. *Polymer* **42**, 3345–3353 (2001).
30. U. Sharma, D. Concagh, L. Core, Y. Kuang, C. You, Q. Pham, G. Zugates, R. Busold, S. Webber, J. Merlo, R. Langer, G. M. Whitesides, M. Palasis, The development of bioresorbable composite polymeric implants with high mechanical strength. *Nat. Mater.* **17**, 96–103 (2018).
31. M. Vatankehah-Varnosfaderani, W. F. M. Daniel, M. H. Everhart, A. A. Pandya, H. Liang, K. Matyjaszewski, A. V. Dobrynin, S. S. Sheiko, Mimicking biological stress–strain behaviour with synthetic elastomers. *Nature* **549**, 497–501 (2017).
32. S. H. Duda, J. Wiskirchen, G. Tepe, M. Bitzer, T. W. Kaulich, D. Stoeckel, C. D. Claussen, Physical properties of endovascular stents: An experimental comparison. *J. Vasc. Interv. Radiol.* **11**, 645–654 (2000).
33. H. Ragelle, M. W. Tibbitt, S.-Y. Wu, M. A. Castillo, G. Z. Cheng, S. P. Gangadharan, D. G. Anderson, M. J. Cima, R. Langer, Surface tension-assisted additive manufacturing. *Nat. Commun.* **9**, 1184 (2018).
34. *Biological evaluation of medical devices - Tests for in vitro cytotoxicity* (ISO standard No. 10993–5, International Organization for Standardization, 2009).
35. *Biological evaluation of medical devices - Sample preparation and reference materials* (ISO standard No. 10993–12, International Organization for Standardization, 2007).
36. L. Novotny, M. Crha, P. Rauser, A. Hep, J. Misik, A. Necas, D. Vondrys, Novel biodegradable polydioxanone stents in a rabbit airway model. *J. Thorac. Cardiovasc. Surg.* **143**, 437–444 (2012).
37. A. Korpela, P. Aarnio, H. Sariola, P. Törmälä, A. Harjula, Comparison of tissue reactions in the tracheal mucosa surrounding a bioabsorbable and silicone airway stents. *Ann. Thorac. Surg.* **66**, 1772–1776 (1998).
38. Y.-K. Chao, K.-S. Liu, Y.-C. Wang, Y.-L. Huang, S.-J. Liu, Biodegradable cisplatin-eluting tracheal stent for malignant airway obstruction: In vivo and in vitro studies. *Chest* **144**, 193–199 (2013).
39. A. Korpela, P. Aarnio, H. Sariola, P. Törmälä, A. Harjula, Bioabsorbable self-reinforced poly-L-lactide, metallic, and silicone stents in the management of experimental tracheal stenosis. *Chest* **115**, 490–495 (1999).
40. J.-P. Nuutinen, C. Clerc, R. Reinikainen, P. Törmälä, Mechanical properties and in vitro degradation of bioabsorbable self-expanding braided stents. *J. Biomater. Sci. Polym. Ed.* **14**, 255–266 (2003).
41. H. Dutau, A. I. Musani, S. Laroumagne, K. Darwiche, L. Freitag, P. Astoul, Biodegradable airway stents—bench to bedside: A comprehensive review. *Respiration* **90**, 512–521 (2015).
42. M. C. Jones, F. A. Rueggeberg, H. A. Faircloth, A. J. Cunningham, C. M. Bush, J. D. Prosser, J. L. Waller, G. N. Postma, P. M. Weinberger, Defining the biomechanical properties of the rabbit trachea. *Laryngoscope* **124**, 2352–2358 (2014).
43. J. Chaure, C. Serrano, R. Fernández-Parra, E. Peña, F. Lostalé, M. A. D. Gregorio, M. A. Martínez, M. Malvé, On studying the interaction between different stent models and rabbit tracheal tissue: Numerical, endoscopic and histological comparison. *Ann. Biomed. Eng.* **44**, 368–381 (2016).
44. S.-Y. Fu, X.-Q. Feng, B. Lauke, Y.-W. Mai, Effects of particle size, particle/matrix interface adhesion and particle loading on mechanical properties of particulate–polymer composites. *Compos. Part B.* **39**, 933–961 (2008).
45. *Biological Evaluation of Medical devices — Tests for local effects after implantation* (ISO Standard No. 10993–6, International Organization for Standardization, 2016).
46. Y. Chen, S. Zhou, Q. Li, Mathematical modeling of degradation for bulk-erosive polymers: Applications in tissue engineering scaffolds and drug delivery systems. *Acta Biomater.* **7**, 1140–1149 (2011).
47. B. G. Amsden, M. Yat Tse, N. D. Turner, D. K. Knight, S. C. Pang, In vivo degradation behavior of photo-cross-linked star-poly( $\epsilon$ -caprolactone-co-D,L-lactide) elastomers. *Biomacromolecules* **7**, 365–372 (2006).
48. S. Li, Hydrolytic degradation characteristics of aliphatic polyesters derived from lactic and glycolic acids. *J. Biomed. Mater. Res.* **48**, 342–353 (1999).
49. P. Willmer, G. Stone, I. Johnstone, *Environmental Physiology of Animals* (Blackwell Publishing, 2005).
50. F.-T. Chung, S.-M. Lin, C.-L. Chou, H.-C. Chen, C.-Y. Liu, C.-T. Yu, H.-P. Kuo, Factors leading to obstructive granulation tissue formation after ultraflex stenting in benign tracheal narrowing. *Thorac. Cardiovasc. Surg.* **58**, 102–107 (2010).
51. W. F. Hosford, *Solid Mechanics* (Cambridge Univ. Press, 2010).
52. A. N. Gent, A new constitutive relation for rubber. *Rubber Chem. Technol.* **69**, 59–61 (1996).

**Acknowledgments:** We thank L. Freitag (Klinik Hirslanden St. Anna, Luzern) for providing helpful technical advices and W. Woigk (ETH Zurich) for assistance in mechanical testing. S. Magdassi and M. Layani (The Hebrew University of Jerusalem) are acknowledged for sharing the original design of the heatable DLP printer. We also thank M. Tibbitt, E. Guzzi (ETH Zurich), and H. Ragelle (Roche) for providing the different designs of the stents used to show 3D printing quality. M. Tegelkamp and H. Richter are acknowledged for assistance in in vivo study. **Funding:** Financial support from the Swiss National Science Foundation (Sinergia project no. 177178) is acknowledged. **Author contributions:** N.P.: design, synthesis, and analysis of polymers; design, execution, and analysis of 3D printing and mechanical testing, degradation, and in vitro studies; preparation of the samples for in vivo study; and led manuscript writing and revision. Y.B.: design, synthesis, and analysis of polymers; and design of dual-polymer resin strategy, resin optimization, overall supervision, and manuscript writing and revision. F.B.C.: design of customized stents, design and production of delivery device and Mylar loop, interpretation, and manuscript revision. K.M.: customization of 3D printer, assistance with study design and mechanical testing, overall interpretation, and manuscript revision. A.K.G. and K.K.: design and execution of in vivo study, analysis, interpretation, and manuscript revision. A.R.: numerical simulations with interpretations and manuscript revision. J.C.: optimization of the resin composition and manuscript revision. P.W.K.: design and execution of in vivo study and manuscript revision. N.K.: customization of 3D printer, assistance with study design, and manuscript revision. A.K.: design of histological processing and evaluation methods, histopathological analysis and interpretation, and manuscript revision. Z.L.: design of gold incorporation strategy and manuscript revision. F.R.: execution of in vivo study and manuscript revision. D.B.: assistance with study design and manuscript revision. B.v.R. and D.F.: design and coordination of in vivo studies, overall interpretation, and manuscript revision. A.R.S.: design and coordination of 3D printing processes and material characterization, overall interpretation, and manuscript revision. J.-C.L.: overall conception, overall design, overall coordination, overall interpretation, and manuscript writing and revision. **Competing interests:** The authors declare that they have no competing interests. **Data and materials availability:** All data needed to evaluate the conclusions in the paper are present in the paper and/or the Supplementary Materials. Additional data related to this paper may be requested from the authors.

Submitted 24 September 2020

Accepted 17 December 2020

Published 3 February 2021

10.1126/sciadv.abe9499

**Citation:** N. Paunović, Y. Bao, F. B. Coulter, K. Masania, A. K. Geks, K. Klein, A. Rafsanjani, J. Cadalbert, P. W. Kronen, N. Kleger, A. Karol, Z. Luo, F. Rüber, D. Brambilla, B. von Rechenberg, D. Franzen, A. R. Studart, J.-C. Leroux, Digital light 3D printing of customized bioresorbable airway stents with elastomeric properties. *Sci. Adv.* **7**, eabe9499 (2021).

## Digital light 3D printing of customized bioresorbable airway stents with elastomeric properties

Nevena Paunovic, Yinyin Bao, Fergal Brian Coulter, Kunal Masania, Anna Karoline Geks, Karina Klein, Ahmad Rafsanjani, Jasmin Cadalbert, Peter W. Kronen, Nicole Kleger, Agnieszka Karol, Zhi Luo, Fabienne Rüber, Davide Brambilla, Brigitte von Rechenberg, Daniel Franzen, André R. Studart and Jean-Christophe Leroux

*Sci Adv* 7 (6), eabe9499.  
DOI: 10.1126/sciadv.abe9499

ARTICLE TOOLS	<a href="http://advances.sciencemag.org/content/7/6/eabe9499">http://advances.sciencemag.org/content/7/6/eabe9499</a>
SUPPLEMENTARY MATERIALS	<a href="http://advances.sciencemag.org/content/suppl/2021/02/01/7.6.eabe9499.DC1">http://advances.sciencemag.org/content/suppl/2021/02/01/7.6.eabe9499.DC1</a>
REFERENCES	This article cites 46 articles, 2 of which you can access for free <a href="http://advances.sciencemag.org/content/7/6/eabe9499#BIBL">http://advances.sciencemag.org/content/7/6/eabe9499#BIBL</a>
PERMISSIONS	<a href="http://www.sciencemag.org/help/reprints-and-permissions">http://www.sciencemag.org/help/reprints-and-permissions</a>

Use of this article is subject to the [Terms of Service](#)

---

*Science Advances* (ISSN 2375-2548) is published by the American Association for the Advancement of Science, 1200 New York Avenue NW, Washington, DC 20005. The title *Science Advances* is a registered trademark of AAAS.

Copyright © 2021 The Authors, some rights reserved; exclusive licensee American Association for the Advancement of Science. No claim to original U.S. Government Works. Distributed under a Creative Commons Attribution License 4.0 (CC BY).